Supporting Information

Self-contact snapping metamaterial for tensile energy dissipation

Sen Yan[a], Zhiqiang Meng[b], Wenlong Liu[a], Xiaojun Tan[c], Peizheng Cao[a], Yongzheng Wen[a], Zheng Xiang[d], Jie Chen[d], Yong Xu[a, e], Yifan Wang[b], Jingbo Sun[a], Lingling Wu[f]*, Ji Zhou[a]**

[a] State Key Laboratory of New Ceramics and Fine Processing, School of Materials Science and Engineering, Tsinghua University, Beijing, 100084, PR China

[b] School of Mechanical and Aerospace Engineering, Nanyang Technological University, Singapore 639798, Singapore

[c] School of Civil Aviation, Northwestern Polytechnical University, Xi'an, 710129, PR China.

[d] Institute of Machinery Manufacturing Technology, China Academy of Engineering Physics, Mianyang 621900, PR China

[e] China Academy of Engineering Physics, Mianyang 621900, PR China

[f] State Key Laboratory for Manufacturing Systems Engineering, Xi'an Jiaotong University, Xi'an, 710049, PR China

*Authors to whom correspondence should be addressed:

jingbosun@mail.tsinghua.edu.cn

lingling.wu@xjtu.edu.cn

zhouji@tsinghua.edu.cn

S1. Theory for SCSM

In our model, we consider the contact in the 2D double-strip model as point contact, which is demonstrated in the FE snapshots in Fig. S3b. Such point contact provides adequate obstruction and induces a transition from low-order to high-order buckling modes predicted by Euler-Bernoulli beam theory (Fig. S3c). Therefore, the deformation process of the double-strip structure can still be explained by the basic buckling mode of Euler-Bernoulli beam theory due to their special contact type. We assume pre-curved distance $\Delta = 0$ and friction coefficient $\mu = 0$ for an idealized model in the following derivation. Under axial end shortening, the strip undergoes buckling. The fourth-order linearized differential equation describing an Euler beam under axial compression is given by[1]

$$\begin{aligned} w^{(iv)}(x) + n^2 w''(x) &= 0 \\ n^2 &= \frac{P}{EI} \end{aligned} \tag{S1}$$

where a prime denotes differentiation with respect to w. $w = w(x)$ describes the centerline deflection of the beam. n is a constant. P is the axial force. I is the beam's moment of inertia, and E is Young's modulus of the material. The boundary conditions of the strips are $w(0) = w(L) = w'(0) = w'(L) = 0$. Next, the eigenvalues n_iL (i = 0,1,2…) are found to solve the equation, and the solutions can be divided into two groups:

$$\begin{aligned} w_i(x) &= \begin{cases} 1-\cos\left(n_i x\right), i = 0,2,4,\ldots, \\ 1-\cos\left(n_i x\right)-\dfrac{2}{n_i L}\left[n_i x-\sin\left(n_i x\right)\right], i = 1,3,5,\ldots, \end{cases} \\ n_i L &= 2\pi, 4\pi, 6\pi, \ldots,\ i = 0,2,4,\ldots \\ n_i L &= 2.86\pi, 4.92\pi, 6.94\pi, \ldots,\ i = 1,3,5,\ldots \end{aligned} \tag{S2}$$

When a force F is applied to the strip, its deflection $y(x)$ can be described as a superposition of these basic buckling modes

$$y(x) = \sum_{i=0}^{n} C_i w_i(x) \tag{S3}$$

where C_i are arbitrary constants, i.e., the amplitudes of the functions. The given strip's length excluding the contraction from the axial load ($L_c + d_0 - d_p$) provides the constraint, where L_c is the current strip's length under compression, d_p is the contraction from the axial load, d_0 refers to the total amount of compression. According to the geometric relation, we obtain the following equation:

$$L_c + d_0 - d_P = \int_0^L \sqrt{1+\left[y'(x)\right]^2}\,dx \approx \int_0^L \left\{1+\frac{\left[y'(x)\right]^2}{2}\right\}dx$$
$$L_c = L - d_0 \tag{S4}$$
$$d_P = \frac{PL}{EA} = \frac{PL}{Ebt}$$

where A is the cross-section area of the beam, t is the strip's thickness, and b is the thickness out of the plane.

As extensively discussed in previous references[2, 3], the first two modes of buckling $w_i(x)$ (i = 0, 1), make predominant contributions to the beam's deformation during buckling. Here, we can depict the specific configurations of two strips through a superposition of $w_1(x)$ and $w_0(x)$ as follows:

$$\begin{cases} y_1(x) = y_2(x) = C_{10}w_0(x), & \text{buckle and before contact} \\ y_1(x) = y_2(x) = C_{20}w_0(x) + C_{21}w_1(x), & x = d_{\text{snap1}} \\ y_1(x) = C_{30}w_0(x), y_2(x) = C_{31}w_1(x), & x = d_{\text{snap2}} \\ y_1(x) = y_2(x) = C_{40}w_0(x), & \text{after contact} \end{cases} \tag{S5}$$

Among them, we can determine the ratio C_0/C_1 in the hybrid buckling mode $C_0w_0(\mathrm{x}) + C_1w_1(\mathrm{x})$ through the deformation of $w_0(\mathrm{x})$ and $w_1(\mathrm{x})$ under equal compression. Then, we obtain the critical compression d_{buckle} for the initial buckling of the two strips. Utilizing geometric relations, we further calculate the critical compression d_{contact} for their contact, and d_{snap1}, d_{snap2} for the first and second snap-through buckling (Fig. S4). The corresponding buckling mode curves predicted by the theoretical analysis are verified by FEA results (Fig. S5). Next, based on buckling mode analysis, we develop a piecewise linear model to describe the multi-step deformation process of the two-strip substructure under compression. Critical buckling forces for the different strip buckling modes are denoted as P_0, P_1, P_2… (n = 1,2,3…). Each critical deformation state can be calculated and transitions between adjacent states are simplified by linearity. The ten stages of the two-strip substructure's mechanical response are shown in Fig. S6 and the corresponding deformation analysis is outlined as follows:

(i) From axial compression to both strips buckling into a low-order buckling mode $w_0(\mathrm{x})$ when the compression force on the two strips reaches $2P_0$.

$$d_1 = \frac{P_0 L}{EA}$$
$$F_1 = \frac{2EA}{L}x, x \in \left[0, d_1\right] \tag{S6}$$

(ii) From both strips buckling to their contact when the compression reaches $x_{contact}$. During this

stage, the compression force F_2 remains constant.

$$\begin{aligned} d_2 &= d_{\text{contact}} \\ F_2 &= 2P_0, x \in (d_1, d_2] \end{aligned} \tag{S7}$$

(iii) The strip's buckling mode w_0(x) beginning to transform when the force arrives $F_3 = 2P_0$. Both strips prefer the high-order antisymmetric buckling mode w_1(x) under constraint boundary conditions.

$$\begin{aligned} d_3 &= d_2 + \frac{(P_1 - P_0)L}{EA} \\ F_3 &= \frac{2P_1 - 2P_0}{d_3 - d_2} x - \frac{2P_1 d_2 - 2P_0 d_3}{d_3 - d_2}, x \in (d_2, d_3] \end{aligned} \tag{S8}$$

(iv) Because of the contact interaction, strips constrain each other until they transform into a superposition of two basic buckling modes, the hybrid buckling mode $C_0 w_0$(x) + $C_1 w_1$(x), under a constant high-order antisymmetric buckling force.

$$\begin{aligned} d_4 &= d_{\text{snap1}} \\ F_4 &= 2P_1, x \in (d_3, d_4] \end{aligned} \tag{S9}$$

(v) Due to a manufacturing defect, the center curves of two strips differ: one strip degrades into w_0(x) accompanied by energy release as the first snap-through buckling, while the other strip maintains its buckling configuration. This rapid process results in subsequent deformation similar to the unequal-thickness strips model we previously studied. The virtual critical compression d_v for one strip's high-order symmetric buckling mode w_2(x) and the low-order buckling mode w_0(x) of the other is first determined:

$$d_v = d_2 + \frac{(P_2 - P_0)L}{EA} \tag{S10}$$

Then, we can get

$$\begin{aligned} F_{\text{snap1}} &= \frac{P_1 - P_2}{d_{\text{snap2}} - d_{\text{v}}} d_5 - \frac{(P_2 + P_0) d_{\text{snap2}} - (P_1 + P_0) d_{\text{v}}}{d_{\text{snap2}} - d_{\text{v}}} \\ F_5 &\in (2P_1, F_{\text{snap1}}], x = d_5 = d_4 \end{aligned} \tag{S11}$$

(vi) In this stage, the asymmetrically deformed strip begins to transform into the high-order asymmetric buckling mode w_1(x) until the compression comes to d_{snap2}, while the symmetrically deformed strip retains the same mode w_0(x).

$$\begin{aligned} d_6 &= d_{\text{snap2}} \\ F_6 &= \frac{P_1 - P_2}{d_6 - d_v} x - \frac{(P_2 + P_0) d_6 - (P_1 + P_0) d_v}{d_6 - d_v}, x \in (d_5, d_6) \end{aligned} \tag{S12}$$

(vii) The asymmetrically deformed strip buckles into $w_1(x)$ and rapidly returns to the opposite low-order buckling mode $-w_0(x)$ with the second`` snap-through buckling. At this time, the force decreases to $F_6 = F_2$ and the displacement d_6 is constant with d_5.

$$F_6 \in \left(P_1 + P_0, 2P_0\right], x = d_7 = d_6 \tag{S13}$$

(viii) After the snap-through buckling, two strips maintain the low-order buckling mode, and the force F_7 remains constant.

$$F_7 = 2P_0, \quad x \in \left(d_7, d_{\text{plastic}}\right) \tag{S14}$$

Where d_{plastic} is the maximum compression displacement of the two strips before plastic deformation.

(ix) Upon unloading, two strips remain in the low-order buckling mode until they recover the initial straight state.

$$F_8 = 2P_0, \quad x \in \left(d_1, d_{\text{plastic}}\right) \tag{S15}$$

(x) The process of axial compression until two strips completely recover their undeformed state.

$$F_{10} = \frac{2EA}{L}x, x \in \left[0, d_1\right] \tag{S16}$$

Next, we adopt the specific damping coefficient to evaluate the effective energy-dissipation performance of metamaterials [4-6]: $\psi = 8U_{\text{dis}}/U_{\text{ideal}}$, where ψ is the specific damping coefficient, U_{dis} is the dissipated energy and U_{ideal} is an ideal dissipation calculated by integrating the minimum rectangular area enclosing the local hysteresis. In contrast to the two-strip model with unequal thickness presented in our previous work[7], the two-strip model with equal thickness exhibits a higher specific damping coefficient due to their more synergistic deformation, as shown in Fig. S7.

S2. FEA of SCSM

The commercial software Abaqus/Standard is utilized for static finite element simulations. As shown in the inset of Fig. S8a, a two-dimensional model of the two-strip substructure is established with a virtual defect to trigger the asymmetric buckling mode of the strip. The simulation adopted the linear elastic material using PLA parameters (E = 2650 MPa, υ = 0.3, and σ_s = 48 MPa) without considering

the viscosity. Vertical compression is applied on the top edge of the two-strip model, while a fixed boundary condition is imposed on its bottom edge. All models are discretized using four-node linear rectangular elements with reduced integration and plane strain (Abaqus type CPE4R) to accurately capture deformation. The mesh size is chosen as 0.2 mm based on convergence analysis. To ensure stable asymmetric buckling, the defect size is selected as $\Delta h/L$ = 6.25e-3. The self-contact interaction is considered by assuming a tangential friction coefficient of 0.5 and hard contact in the normal direction, aligning with experimental results. We adopt the static general algorithm, encompassing loading and unloading analytical steps, and introduce a damping factor of 10^{-12} to expedite the convergence rate. According to the analysis of parameters that the previous theory neglected (Fig. S9), we observe that the concave offset Δ has an impact on both critical compression for two snapping of the two-strip substructure. In contrast, the friction coefficient μ specifically influences the first critical compression for snapping. Fig. S8b depicts the 2D SCSM model for static finite element simulations. In this model, tensile displacement is applied to the top edge, while a fixed boundary condition is imposed on the bottom edge. All other parameter settings are identical to those in the previous two-strip model.

S3. Experiment preparation

To fabricate the samples, we select PLA as the constituent material due to its high stiffness and low viscosity. The measured material properties are obtained in Fig. S10. Additionally, we fabricate the metal sample using $Ni_{50.4}Ti_{49.6}$ power through laser power bed fusion to validate the universality of our design.

For quasi-static experiments, we employ a uniaxial testing machine (AG-IC) with a maximum load cell of 5 kN to measure the displacement-controlled force-displacement relations of the proposed metamaterials at a loading rate of 2 mm/min.

To investigate the dynamic response of the tensile SCSM to impact loading, we develop a custom tensile impact test platform, as shown in Fig. S20. The deployment includes an impactor (doll model), an inelastic rope, a ruler, an acceleration sensor (CT1001L, IPEP, produced by CENGTEC. INC.), and a dynamic data collection device (National Instruments NI 6341 DAQ card and LABVIEW program). The impactor weighing 150 g is connected to the bottom of the sample via the inelastic rope. Various impulse loads can be generated by dropping the impactor from different heights. The accelerometer is rigidly attached to the impactor to measure acceleration data for dynamic analysis. A camera with a framerate of 960 fps captures the deformation process.

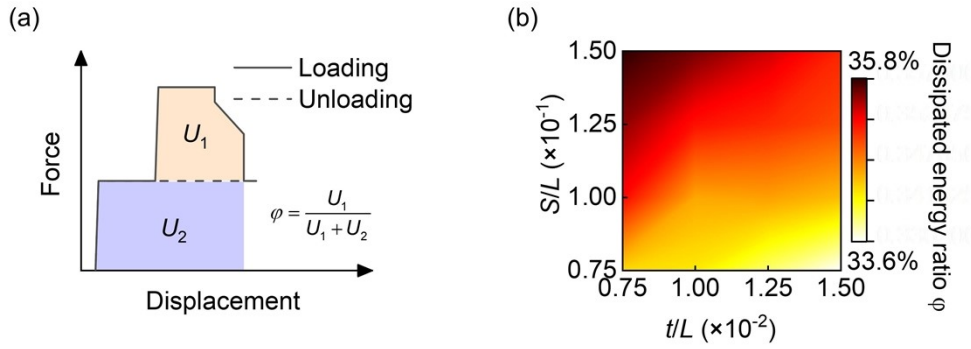

Fig. S1. Calculation of the ratio φ between dissipated energy and strain energy of the two-strip substructure. (a) Schematic for calculating the ratio φ between dissipated energy and strain energy. The orange area, i.e., hysteresis, represents the dissipated energy, while the combined blue and orange areas, beneath the loading curve, indicate the total strain energy. (b) Phase diagram illustrating the dissipated energy ratio φ varying with dimensionless double-strip distance *S*/*L* and dimensionless strip thickness *t*/*L* from theory. The ratio φ slightly increases with increasing *t*/*L* and *S*/*L*, ranging from 33.6% to 35.8%. The minor variation in this parameter is due to both strain energy and dissipated energy exhibit similar trends with changes in structural parameters.

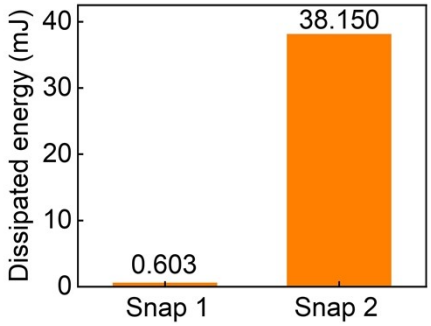

Fig. S2. Energy dissipation from Snap 1 and Snap 2 of two-strip substructure under compression. Snap 2 dissipates much more energy than Snap1 due to the occurrence of a higher buckling mode transition on Snap 2. These results are obtained from FEA.

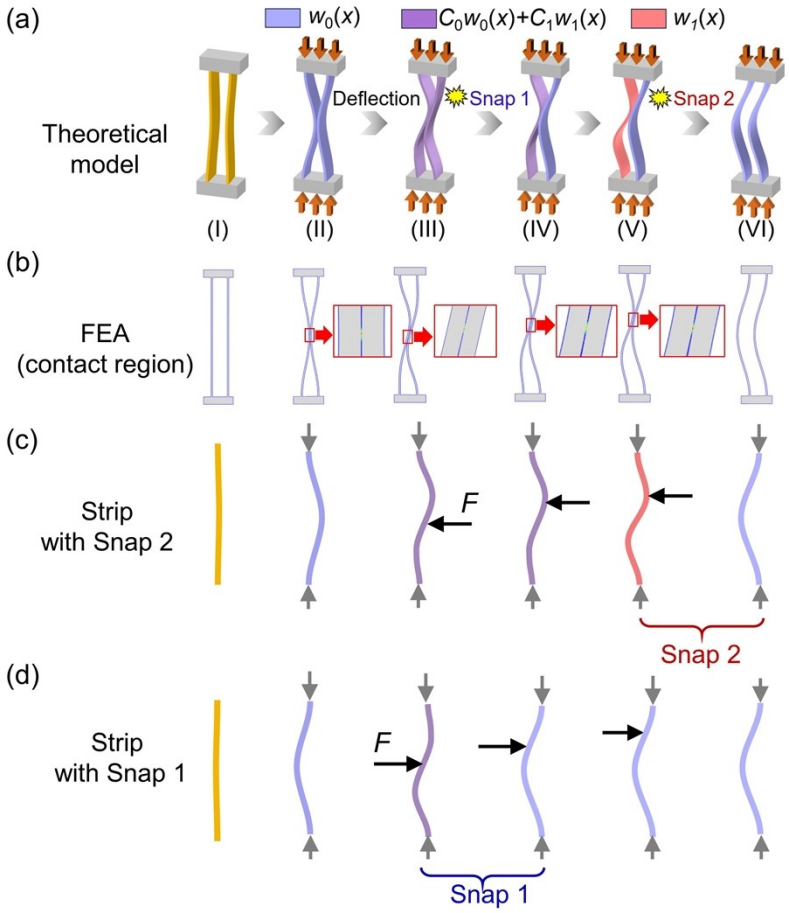

Fig. S3. Contact and buckling mode analysis of the two-strip substructure. (a) Theoretical buckling mode transitions in double-strip structure under compression. (b) Contact analysis in double-strip structure from FEA. (c-d) Theoretical buckling mode transitions in individual interacting strips.

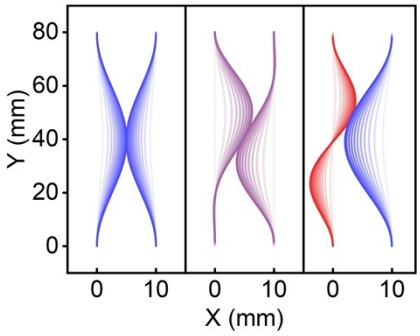

Fig. S4. Centre line deflection curves of two-strip substructure for different critical states. The global position coordinates of the strips are denoted by (X, Y). Three critical buckling configurations corresponding to II, III, and V in Fig. 1e are shown in solid lines, while the initial and intermediate iterations are shown in dotted lines.

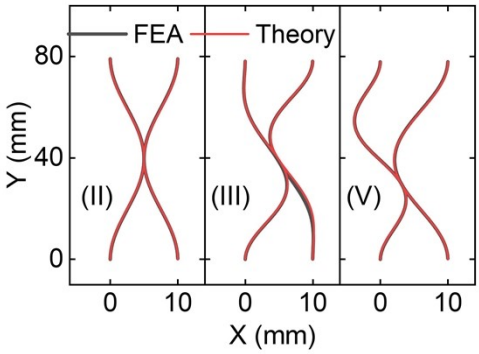

Fig. S5. Shape curves of the interacting strips for different critical states. These curves are extracted from FEA to verify the accuracy theoretical predictions. The numerical labels identify the specific deformation states in Fig. S3.

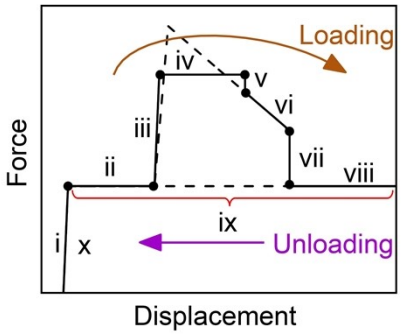

Fig. S6. Force-displacement curve derived from the piecewise linear theoretical model. The dotted line represents the virtual deformation path used to calculate stage vi.

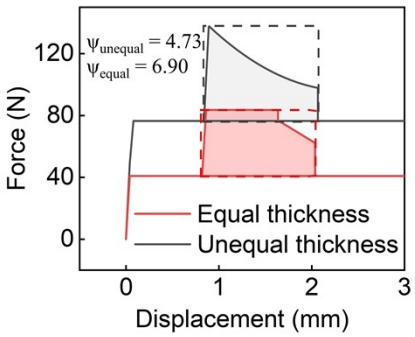

Fig. S7. Force-displacement curves of two equal-thickness strips and two unequal-thickness strips based on theoretical models. The thickness of two equal-thickness strips is t = 1 mm, whereas the thicknesses of two unequal-thickness strips are t_1 = 1 mm and t_2 = 1.4 mm. The dotted rectangular frames represent the ideal energy dissipation of local hysteresis for calculating the specific damping coefficient. The specific damping coefficients can be calculated as $\psi_{unequal}$ = 4.73, and ψ_{equal} = 6.90. The two-strip model with equal thickness exhibits a specific damping coefficient about 45.9% higher than that of the previous two-strip model with unequal thickness.

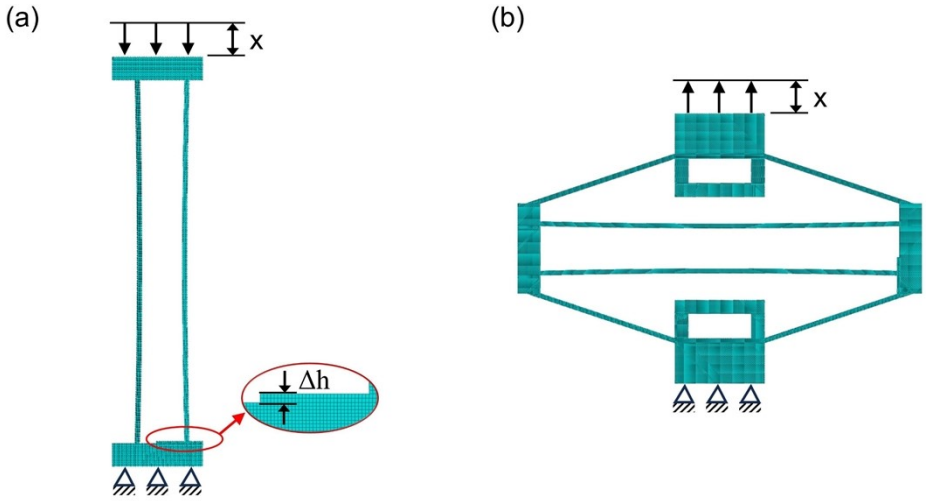

Fig. S8. Depiction of finite element models. Vertical displacement x and clamped boundary conditions are applied on the upper and bottom edges of (a) two-strip models and (b) tensile SCSM models. The virtual defect Δh is introduced to trigger the asymmetric buckling mode.

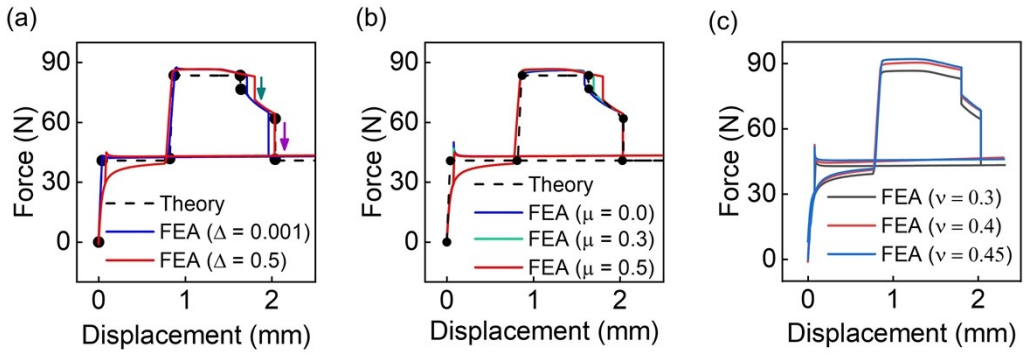

Fig. S9. Effect of (a) concave offset Δ, (b) friction coefficient μ, and (c) Poisson's ratio ν on the mechanical response of two-strip substructure under compression.

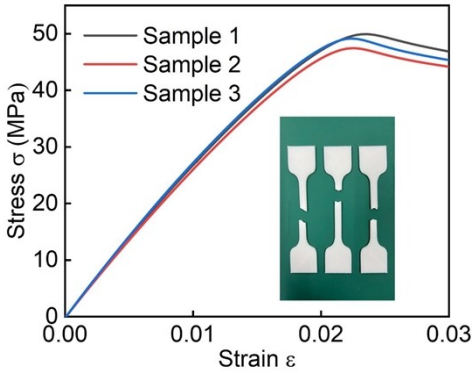

Fig. S10. Stress-strain curves of PLA dog-bone samples obtained from tensile tests. The obtained material properties of PLA are Young's modulus E = 2650 MPa, and yield strength σ_s = 48 MPa.

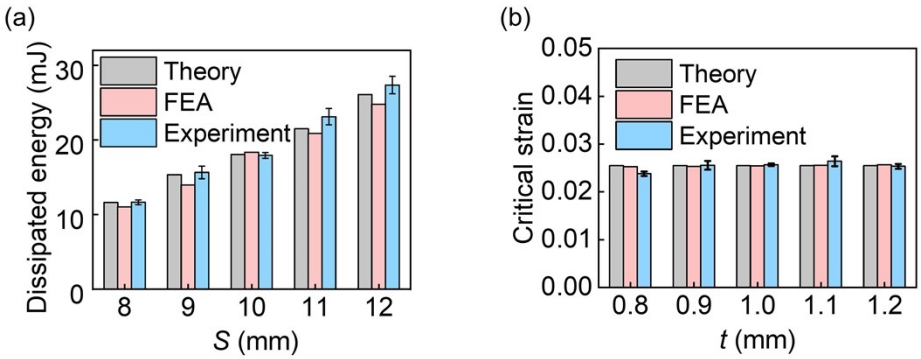

Fig. S11. (a) Effect of the distance S of two strips on energy dissipation density of two-strip substructure under compression. (b) Effect of the strip thickness t on the critical strain ε_{cr} for Snap 2 of the two-strip substructure under compression.

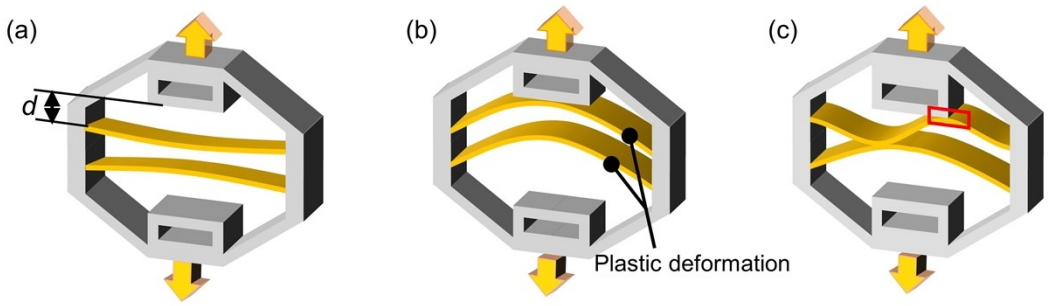

Fig. S12. (a) Limit distance between limit structure and two-strip substructure. (b) Large distance causing excessive deflection (plastic deformation) of strips. (c) Small distance preventing snapping of strips.

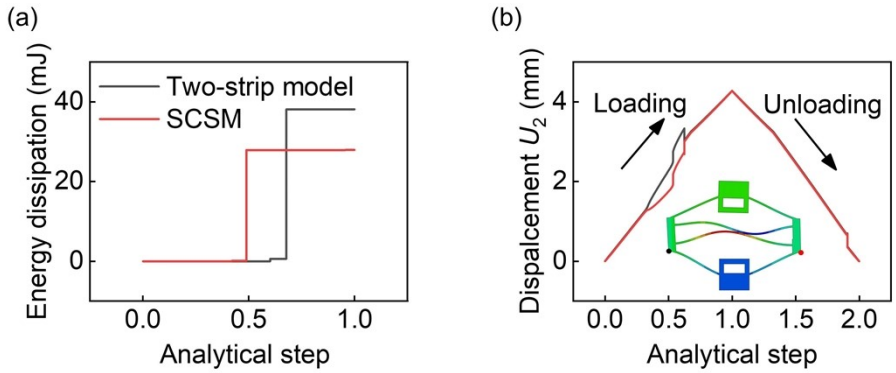

Fig. S13. (a) Analysis of energy dissipation where the SCSM dissipates less energy than a single two-strip structure. (b) Vertical displacement of points on both edges during loading and unloading. The studied points, marked in black and red, correspond to the curves of the same color. Analytical steps involve loading and unloading in FEA. The shear deformation, confirmed by the different vertical displacements of edges in the SCSM, limits its energy-dissipating performance.

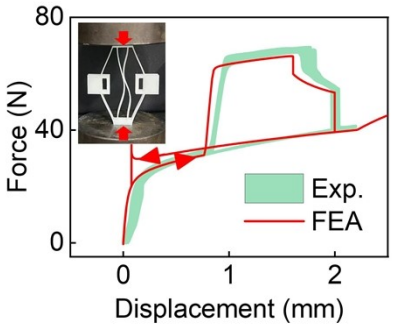

Fig. S14. Force-displacement curves of SCSM unit cell under compression in the *x* direction obtained from experimental results and FEA. The curve exhibits the similarity with that of the two-strip substructure, with the slight increase in stiffness caused by the external frame acting as a linear spring.

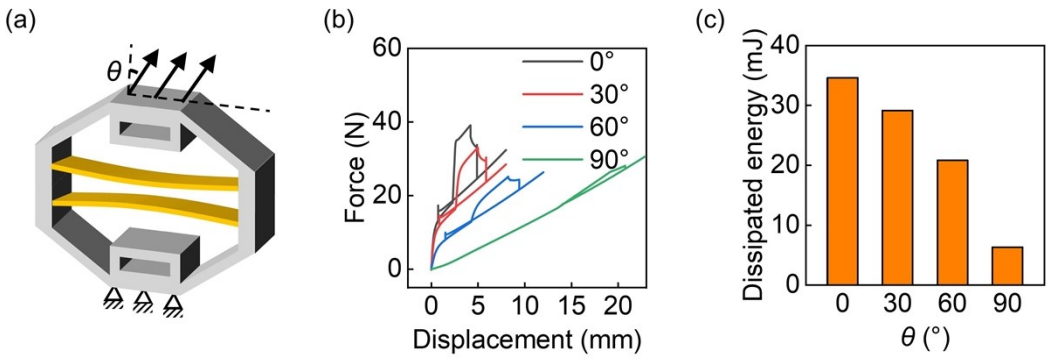

Fig. S15. In-plane inclined tensile force on the SCSM. (a) Schematic diagram of the in-plane inclined tensile force applied to the metamaterial unit cell at an angle θ. (b) Force-displacement curves under inclined loading with different θ obtained from FEA. (c) Dissipated energy of the metamaterial unit cell under inclined tensile force with varying θ.

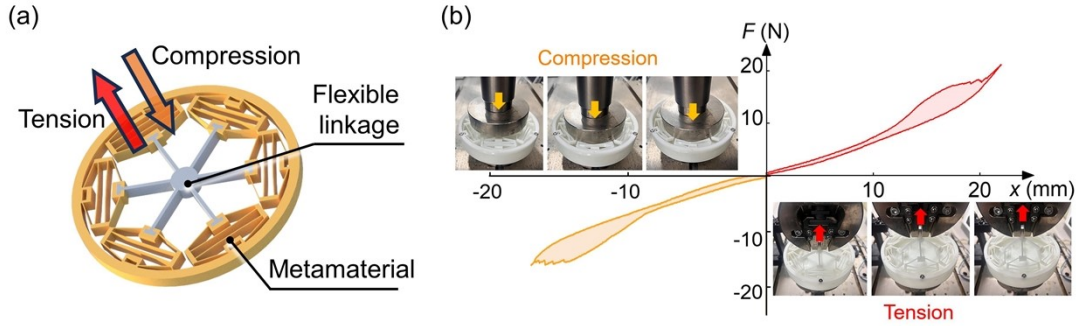

Fig. S16. Out-of-plane deformation of SCSM. (a) The test sample features SCSM unit cells arranged in a circular array, connected by flexible linkages fabricated in TPU. (b) Compression and tension experiments are conducted to assess the out-of-plane deformation of the sample. The mechanical response shows a hysteresis loop induced by sequential snap-through buckling, enabling energy dissipation in both tension and compression.

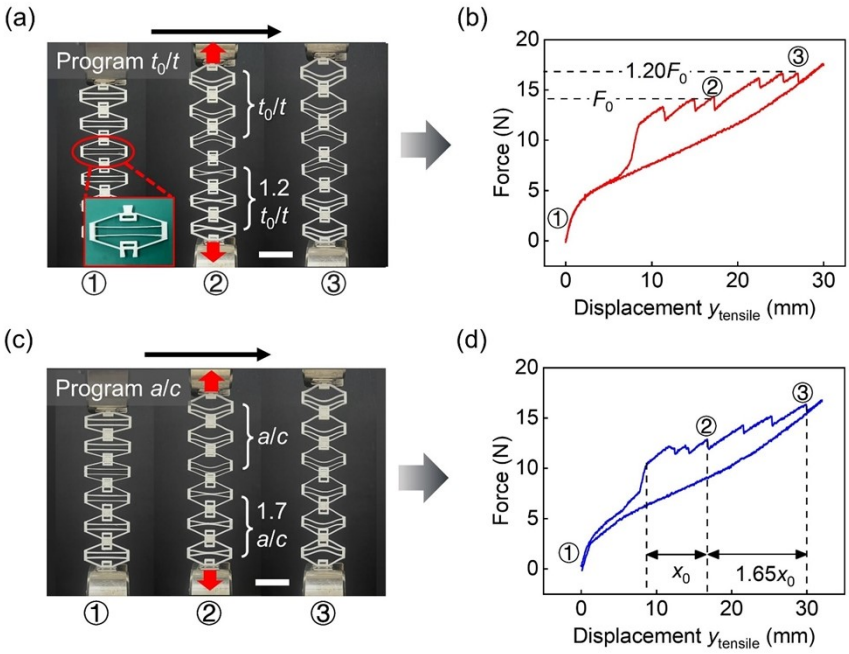

Fig. S17. Programmable modular design of SCSM. (a) Programing parameter t_0/t of SCSM for multiple force thresholds. The insect diagram depicts the SCSM modular with t_0/t = 1.2. (b) Corresponding force-displacement curve exhibiting multiple force thresholds. (c) Programing parameter a/c of SCSM for multiple strain thresholds. The parameter is set to a/c = 4. (d) Corresponding force-displacement curve exhibiting multiple critical strains. The numerical labels in (c-d) correspond to specific deformation states in (a-b), respectively. Other unspecific parameters are consistent with those in Fig. 4a. Scale bar, 3 cm.

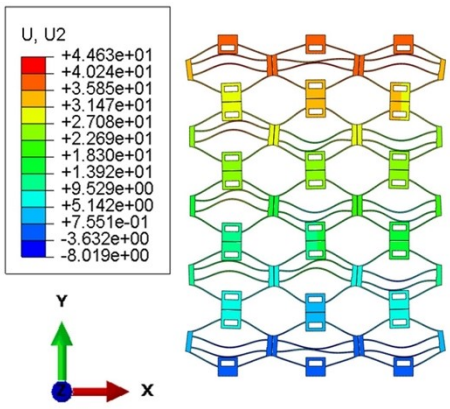

Fig. S18. Transverse coupling deformation of SCSM. Certain unit cells at the edges are unable to undergo snap-through buckling due to nonuniform deformation.

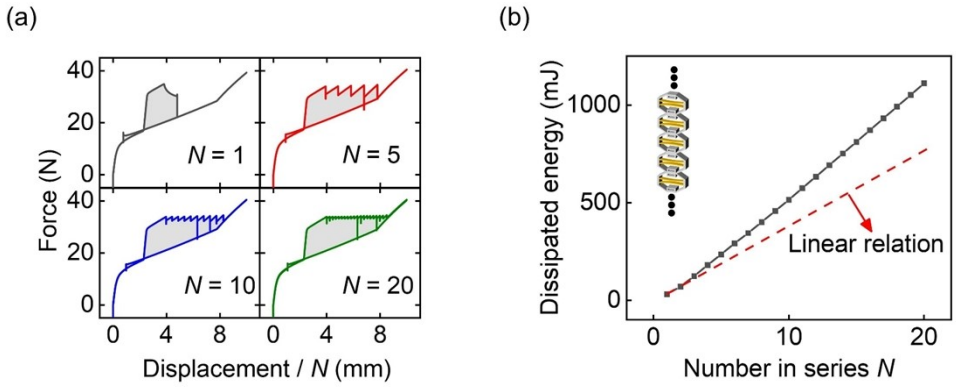

Fig. S19. (a) Mechanical responses of SCSM with different numbers of serial unit cells. (b) Energy dissipation of SCSM with different numbers of serial unit cells. The linear relation is determined by the first two serial unit cells for comparison. The energy dissipation of the SCSM increases nonlinearly with the number of unit cells, which is attributed to the coupled vibration between multiple unit cells, known as the snap-back mechanism discussed in previous literature.[8, 9]

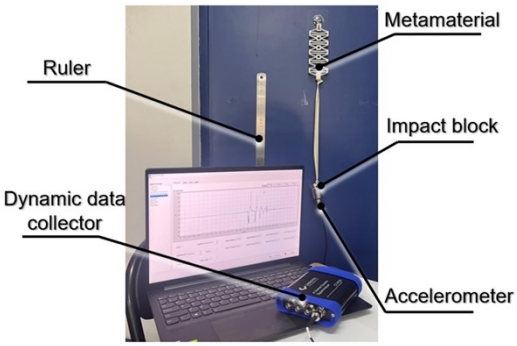

Fig. S20. Schematic diagram of impact testing platform.

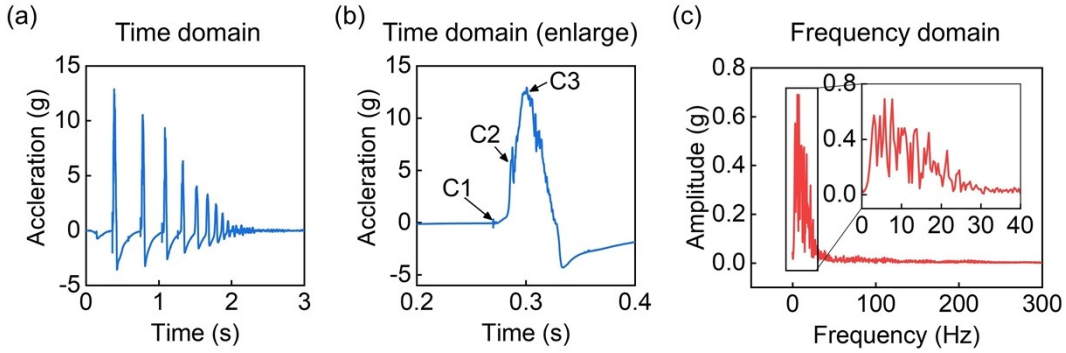

Fig. S21. Dynamic response during impact at releasing height $H = 30$ mm. (a-b) Acceleration-time curve with an enlarged section. C1) The moment when the rope is fully stretched. C2) The sequential snap-through buckling occurs, resulting in a sharp decrease in acceleration. C3) The deformation at the peak acceleration where all strips have snapped. (c) Acceleration amplitude-frequency curve obtained via fast

Fourier transform. The impact acceleration is mainly concentrated in the low frequency-band.

References

1. M. Vangbo, *Sensors Actuat. A: Phys.*, 1998, 69, 212-216.
2. W. Yan, Y. Yu and A. Mehta, *Theor. Appl. Mech. Lett.*, 2019, 9, 264-272.
3. P. Cazottes, A. Fernandes, J. Pouget and M. Hafez, *J. Mech. Design*, 2009, 131, 101001.
4. B. Haghpanah, A. Shirazi, L. Salari-Sharif, A. G. Izard and L. Valdevit, *Extreme Mech. Lett.*, 2017, 17, 56-61.
5. S. Zhu, B. Wang, X. Tan, J. Hu, L. Wang, Z. Zhou and S. Chen, *Compos. Struct.*, 2021, 262, 113381.
6. S. Zhu, B. Wang, L. Chen, X. Tan and L. Ma, *Int. J. Mech. Sci.*, 2022, 213, 106803.
7. S. Yan, W. Liu, X. Tan, Z. Meng, W. Luo, H. Jin, Y. Wen, J. Sun, L. Wu and J. Zhou, *Mater. Today*, 2024, DOI: https://doi.org/10.1016/j.mattod.2024.06.003.
8. D. Restrepo, N. D. Mankame and P. D. Zavattieri, *Extreme Mech. Lett.*, 2015, 4, 52-60.
9. Y. Chen and L. Jin, *Adv. Funct. Mater.*, 2021, 31, 2102113.